OH as a probe of the warm-water cycle in planet-forming disks

Zannese, M.; Tabone, B.; Habart, E.; Goicoechea, J.R.; Zanchet, A.; Dishoeck, E.F. van; ... ; Wolfire, M.G.

nature astronomy

Article

https://doi.org/10.1038/s41550-024-02203-0

OH as a probe of the warm-water cycle in planet-forming disks

Received: 29 July 2023

Accepted: 12 January 2024

Published online: 23 February 2024

Check for updates

A list of authors and their affiliations appears at the end of the paper

Water is a key ingredient for the emergence of life as we know it. Yet, its destruction and reformation in space remain unprobed in warm gas ($T > 300$ K). Here we detect with the James Webb Space Telescope the emission of the hydroxyl radical (OH) from d203-506, a planet-forming disk exposed to external far-ultraviolet (FUV) radiation. These observations were made as part of the Early Release Science programme PDRs4All, which is focused on the Orion bar. The observed OH spectrum is compared with the results of quantum dynamical calculations to reveal two essential molecular processes. The highly excited rotational lines of OH in the mid-infrared are telltale signs of H_2O destruction by FUV radiation. The OH rovibrational lines in the near-infrared are attributed to chemical excitation by the key reaction $O + H_2 \rightarrow OH + H$, which seeds the formation of water in the gas phase. These results show that under warm and irradiated conditions, water is destroyed and efficiently reformed through gas-phase reactions. We infer that, in this source, the equivalent of Earth oceans' worth of water is destroyed per month and replenished. This warm-water cycle could reprocess some water inherited from cold interstellar clouds and explain the lower deuterium fraction of water in Earth's oceans compared with that found around protostars.

Water is a key ingredient in the emergence of life and is, therefore, a key aspect in the assessment of the habitability of (exo)planets. Yet, the trail of water to planets remains unclear. In a disk's inner regions ($\lesssim$10 au), where the terrestrial and sub-Neptune planets are expected to form, a notable fraction of the water inherited from cold interstellar clouds is destroyed and reformed[1–3]. In fact, theoretical models predict that under the warm ($T > 300$ K) and far-ultraviolet (FUV, $6 < h\nu < 13.6$ eV) irradiated conditions present in disk atmospheres, water is destroyed and reformed by the chemical cycle: $O \rightleftarrows OH \rightleftarrows H_2O$ (refs. 1–3). Notably, this cycle is one of the processes that could lower the deuterium-to-hydrogen enrichment of water inherited from cold clouds and explain the intermediate D/H ratio found in Earth's oceans[4].

In the past, understanding the detailed balance between the formation and destruction processes in a protoplanetary disk has been challenging because of the limited observational information. Warm water has been detected in planet-forming disks with Spitzer-IRS[5–7] and ground-based instruments[8], but its ongoing chemistry remains unprobed. Here, we unveil the water cycle under warm and irradiated conditions thanks to the combination of observations of OH made by the James Webb Space Telescope (JWST) and quantum dynamical calculations.

The observational data stem from the JWST Early Release Science (ERS) programme PDRs4All[9], which performed spectroscopic observations of the Orion bar, the edge of an interstellar cloud exposed to the intense FUV radiation from the massive stars of the Trapezium cluster[10] (the FUV flux at the ionization front is $2–7 \times 10^4$ times that of the local interstellar medium[11]). The Solar System presumably formed in a similar environment in which external UV radiation influenced the temperature, mass budget and chemical composition of the solar nebula[12]. Figure 1 shows the d203-506 disk within the observed area as a dark lane against the bright background of the nebulae (see Methods for its detailed characteristics). A photo-evaporative wind, seen as a more diffuse emission of H_2, is launched from the upper layers of the disk[13]. This is the result of the intense FUV radiation from the massive stars in the proximity of d203-506, which heats the gaseous disk. In addition, the young star at the centre launches a collimated

e-mail: marion.zannese@universite-paris-saclay.fr

https://doi.org/10.1038/s41550-024-02203-0

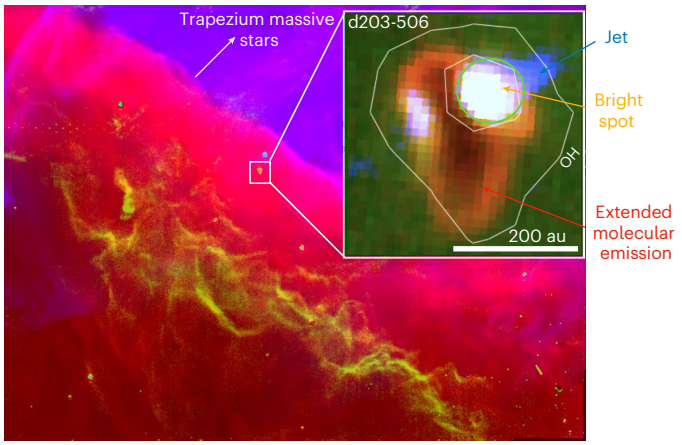

Fig. 1 | JWST NIRCam composite image of the Orion bar in the Orion molecular cloud. Red is the 3.35 μm emission (F335M NIRCam filter), blue is the emission of Paα (F187N filter subtracted by F182M filter) and green is the emission of the H_2 0–0 S(9) line at 4.70 μm (F470N filter subtracted by F480M filter). The inset shows an enlargement of the d203-506 planet-forming disk where OH lines are detected. Red is the emission of the H_2 1–0 S(1) line at 2.12 μm (F212N filter), blue is the [Fe II] line emission at 1.64 μm (F164N filter) and green is the emission in the F140M broadband near-IR filter that traces scattered light around 1.4 μm (F140M broadband filter). The white contours represent the emission of the OH rotational line at 9.79 μm detected with MIRI-MRS (levels are 1.1 and 2.5×10^{-5} erg cm^{-2} s^{-1} sr^{-1}). The bright spot in the northwestern part of the d203-506 system coincides with the region of interaction between a jet and the photo-evaporative wind. The brightest OH emission originates from here. The spectra in Figs. 2 and 3 are averages over the region delineated by the green circle to give the best signal-to-noise ratio. Image credits: NASA, European Space Agency (ESA), Canadian Space Agency (CSA) and PDRs4All ERS Team (pdrs4all.org).

high-velocity jet, seen in [Fe II] line emission, which carves out a cavity in the wind. The northwest part of the cavity is particularly bright in excited molecular lines. This enhanced emission is probably due to a local increase in density induced by jet bow shocks[14] and the direct irradiation from the Trapezium stars or the central star itself. Here, we report the detection of infrared (IR) rotational and rovibrational emission from OH by both MIRI-MRS and NIRSpec, respectively. The OH emission is detected where there is bright H_2 emission, namely all over the photo-evaporative wind, revealing active gas-phase oxygen chemistry fuelled by warm H_2 (Extended Data Fig. 1). In this study, we focus on the bright spot to obtain high signal-to-noise spectra.

Evidence for H_2O photodissociation

The MIRI-MRS spectrum shown in Fig. 2 reveals a series of highly excited rotational lines of OH in the ground vibrational state, corresponding to a change in rotational quantum number of $N \rightarrow N-1$ (see line intensities in Extended Data Table 1 and processing steps in Extended Data Fig. 2). In total, lines from 23 rotational levels from $N = 44$ down to $N = 18$ are detected in the 9–16 μm region, which probes upper-level energies as high as 43,000 K (Extended Data Fig. 3). The excitation diagram of OH reveals an extremely high excitation temperature of 10,000 K. This is ten times larger than the gas temperature inferred from the H_2 rotational lines (Extended Data Figs. 4 and 5). The detection of extremely rotationally excited OH is the smoking gun of water photodissociation. As already acknowledged from previous Spitzer observations[15–17] based on seminal molecular physics studies[18,19], the only process that can excite these lines is H_2O photodissociation through its $\tilde{B}$ electronic state by short-wavelength FUV photons to form OH in high-N states. The levels that are directly populated by water photodissociation ($N \simeq 35$–45) were not detected before due to the limited spectral resolution and sensitivity of Spitzer-IRS. Furthermore, the higher spectral resolution of MIRI-MRS allows us to separate the symmetric from the antisymmetric component of each rotational line down to 9.4 μm (Fig. 2 and Extended Data Fig. 3). Compared with the less-excited lines observed with Spitzer[17], we find a much higher ratio (≥10) between the symmetric and antisymmetric lines. This is consistent with recent quantum calculations using a full-dimensional wave packet method that attributes this propensity to the $\tilde{B} \rightarrow X$ conical intersection pathway[20].

To analyse the MIRI-MRS spectrum, synthetic JWST spectra were computed using the GROSBETA code[21], which takes into account the production of OH in excited states (Methods). As an input, we use the state distribution of nascent OH produced by H_2O photodissociation through its first two electronic states as computed by refs. 19,22. As shown in Fig. 2, the model agrees well with the observed spectrum. In particular, we recover the steep increase in line intensity from $\lambda = 9.15$ μm onward and the relatively constant line intensities beyond 9.5 μm. This behaviour is intrinsically related to the rotational distribution of nascent OH (Extended Data Fig. 6). Once an OH molecule is formed in a rotationally excited state, it decays by $N \rightarrow N-1$ radiative transitions in a process called 'radiative cascade'[21]. The agreement between the model and the observations is not only an astronomical confirmation of a basic molecular process but, as shown below, also provides access to the destruction rate of water and its local abundance.

Evidence for chemical (formation) pumping by O + H_2

The $v = 1 \rightarrow 0$ rovibrational lines of OH are detected at shorter near-IR wavelengths by NIRSpec, with upper rotational quantum numbers from $N = 1$ up to 10 (see Fig. 3, Extended Data Fig. 3, line intensities in Extended Data Table 1 and processing steps in Extended Data Fig. 2). These transitions have been detected in very dense environments, like the innermost regions of protoplanetary disks[8] ($n_H \gtrsim 10^8$ cm^{-3}), but not in a lower-density environment such as the outer layers of the d203-506 system. The excitation of the rotational levels within the $v = 1$ state is well described by a single excitation temperature of about 1,000 K (Extended Data Fig. 5), which is close to the gas temperature inferred from H_2 emission (Extended Data Fig. 4 and Extended Data Table 2) and ten times smaller than the excitation temperature of the mid-IR lines, thus implying a different origin.

We attribute the near-IR OH lines to formation pumping through the reaction O + H_2, which is known to produce OH in vibrationally excited states[23] but has hitherto never been observed in space. We amended the GROSBETA model to include the excitation of OH by the O + H_2 reaction using the state distribution of nascent OH extracted from the recent quantum calculations of ref. 24 (Methods and Extended Data Fig. 6). Since the state distribution of nascent OH depends on both the gas temperature and the state distribution of $H_2(v,J)$, we used the observed lines of H_2 to compute, self-consistently, the distribution of nascent OH. The synthetic GROSBETA model shows good agreement with the NIRSpec spectrum (Fig. 3). The OH $v = 2 \rightarrow 1$ lines are also predicted to be an order of magnitude weaker, in line with the upper limit set by the observations; quantum calculations predict that 20% of the OH is produced in the $v = 1$ state, with less than 1% in higher excited vibrational states ($v \geq 2$). The emission process is relatively simple, as an OH product formed in a $v = 1$ state rapidly cascades down through the rovibrational transitions. Other processes are known to produce OH in vibrational states (UV pumping, H_2O photodissociation through its $\tilde{A}$ electronic state and IR pumping; see Methods and Extended Data Fig. 7), but we find that only inelastic collisions could contribute to the observed emission if OH is very abundant ($x(\mathrm{OH}) \gtrsim 10^{-5}$; see the detailed discussion in Methods). The good agreement between the observations and the model points to formation pumping of OH, thereby supporting an earlier proposal based on Spitzer-IRS and Herschel observations[17,25].

Warm gas-phase oxygen chemistry in action

Because the newly formed OH products immediately decay by the observed transitions, the fluxes of these lines are directly proportional to the formation rate of OH by either route (see Table 1 and Methods for

https://doi.org/10.1038/s41550-024-02203-0

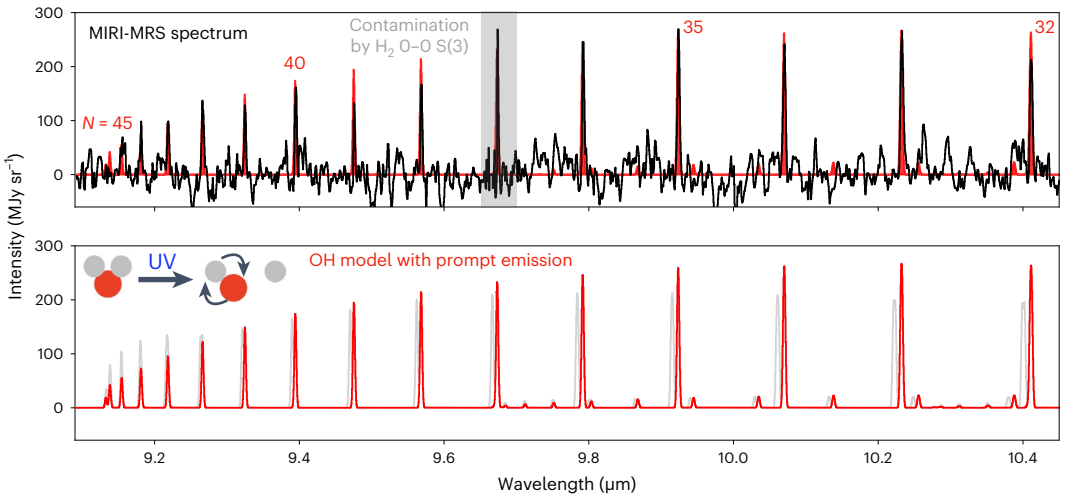

Fig. 2 | Evidence for H_2O photodissociation from OH rotational lines detected by MIRI-MRS. Top: observed MIRI-MRS spectrum. The dust continuum and bright lines, other than that from OH, have been subtracted (Methods and Extended Data Fig. 2). Rotationally excited OH lines are detected up to levels $N = 44$. Bottom: synthetic spectra from GROSBETA. The spectrum in red assumes that water photodissociation produces OH in symmetric Λ-doubling states, whereas the grey spectrum assumes that there is an equal distribution among the sublevels.

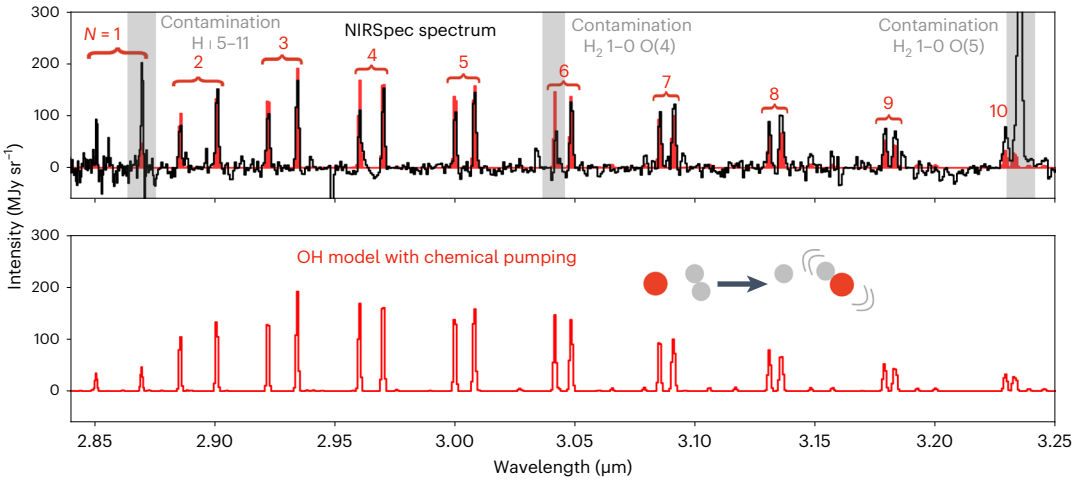

Fig. 3 | Evidence for formation pumping through O + H_2 from OH rovibrational lines detected by NIRSpec. Top: Observed NIRSpec spectrum. The dust continuum and the bright lines, other than those from OH, have been subtracted (Methods and Extended Data Fig. 2). Each rovibrational transition is split by the spin–orbit coupling. However, the Λ doubling is unresolved. Bottom: Synthetic spectra from GROSBETA including the excitation of OH by formation pumping.

further details). From the mid-IR lines, we derive an amount of water photodissociated per unit of time of $\Phi = 1.1 \times 10^{10}$ cm^{-2} s^{-1}. Considering the size of the bright spot (1.53×10^{-12} sr, which is at a distance of 414 pc; ref. 26), this corresponds to, roughly, the equivalent of the Earth oceans' worth of water being photodestroyed per month (the oceans of the Earth are composed of about 5×10^{46} molecules of water). Similarly, from the near-IR lines, we infer an amount of OH formed through O + H_2 per unit of time of $R = 1.2 \times 10^{11}$ cm^{-2} s^{-1}.

These formation rates shed new light on the water cycle under warm and irradiated conditions. The mid-IR lines of OH reveal that water is actively photodestroyed in the d203-506 system. Water lines are not detected with MIRI-MRS, as predicted by non-local thermodynamic equilibrium models (Extended Data Fig. 8), probably due to the low density of the gas, which is much lower than the critical densities of the H_2O transitions observable with JWST. Yet, from the amount of H_2O photodissociated per second, we infer a substantial amount of unseen H_2O in the warm gas with $N(H_2O) \simeq 1–5 \times 10^{15}$ cm^{-2} (Methods). This quantity is still two orders of magnitude too low for water UV shielding in this environment[27]. As estimated from the local FUV radiation field, the destruction timescale of water is about a day, much shorter than the dynamical timescale of the outflowing gas, which is longer than half a century (Methods). Therefore, the illuminated water cannot originate from inherited water formed in cold conditions. In fact, our analysis of the near-IR lines of OH demonstrates that the formation rate of OH from O + H_2 is an order of magnitude larger than the destruction rate of H_2O. Water is, thus, efficiently replenished by the gas-phase formation route initiated by the reaction O + H_2 → OH + H. Our estimates also indicate that only a small fraction of OH, about $\Phi/R \simeq 10\%$, is effectively converted into H_2O. Notably, OH is also photodissociated, reducing the probability of OH being converted into H_2O. Interestingly, OH photodissociation has already been unveiled by Hubble Space Telescope observations of [O I] emission at $\lambda = 6{,}300$ Å (ref. 28), which is probably excited by OH photodissociation[29]. Assuming that [O I] emission is produced through OH + $h\nu$ → O + H with a 50% probability of forming oxygen in the O(^1D) state[30], we infer an amount of OH photodissociated per unit of time of 7×10^{10} cm^{-2} s^{-1}, a value close to the formation rate R through O + H_2 given above.

Table 1 | Parameters derived from the analysis of OH and H_2 lines

Diagnostics	Quantity	Measured value
H_2 lines	$N(H_2)$[a]	$(9.9\pm0.9)\times10^{19}$ cm^{-2}
	T[a]	950±17 K
OH mid-IR lines	Φ (rate $H_2O+h\nu$)[b]	$(1.1\pm0.2)\times10^{10}$ cm^{-2} s^{-1}
	$N(H_2O)$	1×10^{15} to 5×10^{15} cm^{-2}
	$x(H_2O)$[c]	5×10^{-6} to 2.5×10^{-5}
OH near-IR lines	R (rate $O+H_2$)[b,d]	$(1.2\pm0.3)\times10^{11}$ cm^{-2} s^{-1}
	n_H[d]	$(1.4\pm0.4)\times10^{7}$ cm^{-3}

[a]The uncertainties of these values do not take into account calibration effects. They could be increased by a factor of 2–3 if the uncertainty associated with calibration effects is equal to 20%. [b]Number of OH molecules formed per unit area and time by either formation route (in cm^{-2} s^{-1}). [c]The abundance with respect to the total number of hydrogen atoms is calculated using $N(H_2)$ inferred from H_2 lines. [d]The inferred value would be reduced if inelastic collisional excitation were to play an important role. The lower limits expected for these values are $R=1.1\times10^{10}$ cm^{-2} s^{-1} and $n_H=1.3\times10^{6}$ cm^{-3}.

What are the implications for the trail of water to terrestrial planets and notably to Earth?

The enhanced D/H ratio in standard mean ocean water[31] of 1.5×10^{-4} relative to the bulk interstellar elemental D/H ratio ($\sim2\times10^{-5}$)[32] indicates that a fraction of terrestrial water formed under cold conditions, probably at the surface of interstellar grains[33]. This anomaly would indeed reflect the effects of chemistry at low temperatures, for which the small zero-point energy difference between D- and H-bearing species can create large deuterium fractionations[34,35]. However, the observed D/H ratio in protostars[36–38], which traces the inherited water content, is higher than the D/H ratio in standard mean ocean water ($0.3–1\times10^{-3}$ versus 1.5×10^{-4}, respectively). Hence, chemical processing could have occurred in warm gas and reduced the deuterium fractionation because the formation rates of HDO and H_2O are similar at high temperatures. In the d203-506 system, H_2O is efficiently destroyed and reformed through the warm gas-phase formation route $O \rightleftarrows OH \rightleftarrows H_2O$. This can decrease the water D/H ratio inherited from the cold phase to interstellar elemental values ($\sim2\times10^{-5}$)[32]. The resulting HDO/H_2O ratio could be even lower if selective photodissociation of dihydrogen leads to subsolar values of HD/H_2 (ref. 39). It is, however, unclear whether water unveiled in the d203-506 system is incorporated into comets and asteroids since the observed OH might rather trace unbounded gas heated by the external FUV radiation. The latter is further supported by models of photo-evaporative winds with similar conditions as d203-506, which predicts photodissociated OH (and consequently H_2O) to be primarily present in the unbounded gas[40].

Nevertheless, the d203-506 system constitutes a unique interstellar laboratory as the same chemical processes will occur in the atmosphere of planet-forming disks, even if the disk is irradiated solely by the host star. The FUV fields generated by accreting stars at the disk surface range from $G_0=10^3$ to 10^6 between 1 and 10 au, depending on the dust properties and shielding by the gas[3,27], a range that is comparable to that of the gas probed by our observations. The local density inferred from OH mid-IR lines (Methods) is somewhat lower compared with gas densities expected in disk upper layers ($0.2–1.2\times10^7$ cm^{-3} versus $10^8–10^{12}$ cm^{-3}), and the temperature is higher than that found for water in planet-forming disks (1,000 K versus 400–600 K)[7]. Still, the warm gas-phase formation route is already efficient at $T>400$ K and the gas density affects only the relative OH/H_2O ratio in the irradiated layers[41].

We expect mid- and near-IR emission of OH to be detected by JWST in a wide range of astrophysical environments (for example, shocks, photodissociation regions at the edge of molecular clouds and comets). Our new analysis method for OH lines will provide vital constraints on the physics and chemistry of the gas in such environments. This work also constitutes a benchmark illustration of the potential of excited IR lines from small molecular species, which can be transposed to other species like CO, CH^+ (ref. 42) and CH_3^+. In this context, new quantum dynamical calculations and laboratory experiments are essential for exploiting the full potential of JWST.

Methods

Observations and data reduction

Observations with MIRI-MRS in integral field unit mode were obtained as part of the ERS programme PDRs4All: Radiative feedback from massive stars (ID1288, PIs: Berné, Habart, Peeters)[9]. The observations cover a 9 × 1 mosaic centred on α_{J2000} = 05 h 35 min 20.4749 s, δ_{J2000} = −05° 25' 10.45". A four-point dither optimized for extended sources was applied and the FASTR1 readout pattern adapted for bright sources was used. The integration time was 521.7 s using 47 groups per integration and four integrations. The data span a wavelength range from 4.90 to 27.9 μm and have a spectral resolution $R\approx1{,}700–3{,}700$ and a spatial resolution of 0.2–0.8". The latter corresponds to a very small spatial scale of about 100 au at the distance of the Orion bar (414 pc; ref. 26). The MIRI-MRS data were reduced using v.1.11.1 of the JWST pipeline (https://jwst-pipeline.readthedocs.io/en/latest/) and context 1097 of the JWST Calibration Reference Data System (https://jwst-crds.stsci.edu/). The stage 2 residual fringe correction was applied in addition to the standard fringe correction step. A master background subtraction was applied in stage 3 of the reduction. The 12 cubes (four channels of three subbands each), all pointing positions combined, were stitched into a single cube (A.C. et al., manuscript in preparation) (see ref. 47 for data reduction details). The mosaic was positioned to overlap with observations of the Orion bar by the PDRs4All NIRSpec integral field unit, which also produced a 9 × 1 mosaic. The NRSRAPID readout mode appropriate for bright sources and a four-point dither pattern were also used for NIRSpec. The on-source integration time was 257.7 s per exposure with five groups per integration with one integration per exposure. The data were reduced using the JWST Science Calibration Pipeline (v.1.10.2.dev26+g8f690fdc) and the context jwst_1084.pmap of the Calibration Reference Data System (see ref. 11 for the data reduction process). The MIRI-MRS and NIRSpec spectrum, in units of MJy sr^{-1}, were averaged in a circular aperture centred on α_{J2000} = 05 h 35 min 20.3145 s and δ_{J2000} = −5° 25' 05.528" with a radius of 0.15". An OFF position was averaged in a circular aperture centred on α_{J2000} = 05 h 35 min 20.2539 s and δ_{J2000} = −5° 25' 05.498" with a radius of 0.3".

Post-processing of the JWST spectra

To better visualize the OH lines in Figs. 2 and 3, the continuum was subtracted by considering several points in the spectral regions free of line emission. Lines other than that of OH were removed, as shown in Extended Data Fig. 2. In the selected MIRI-MRS spectral range (9–10.4 μm), several prominent lines are present, such as the H I lines 8–13 at 9.261 μm and 9–20 at 9.392 μm and the H_2 0–0 S(3) line at 9.665 μm. The lines from the background of the planet-forming disk were subtracted by fitting them in the OFF spectrum. This allowed us to subtract the emission of the recombination lines of H I, 8–13 at 9.261 μm and 9–20 at 9.392 μm. We also subtracted the H_2 0–0 S(3) line by fitting it directly in the ON spectrum (Extended Data Fig. 2). The same processing was applied to the NIRSpec spectrum. A continuum was subtracted. Then, the H I lines 5–11 at 2.873 μm and 5–10 at 3.039 μm, O I lines at 2.893 and 3.099 μm, H_2 lines 2–1 O(3) at 2.974 μm, 1–0 O(4) at 3.004 μm, 2–1 O(4) at 3.189 μm and two unidentified lines at 3.164 and 3.224 μm were removed by fitting them directly in the ON spectrum.

Characteristics of the planet-forming disk d203-506

The d203-506 system is an almost edge-on disk seen in silhouette against the bright background. Its measured radius is $R_{out}=98\pm2$ au, and its total mass is estimated to be about ten times the mass of

Jupiter[48]. Kinematic studies with ALMA[48] indicate that the stellar mass of the host star is below 0.3 $M_\odot$. This is the archetype of a young planet-forming environment that is in the intermediate phase between being embedded and being unshielded in the surrounding H I gas irradiated by an external FUV field. d203-506 shows no signs of having an ionization front[28,29,48], indicating that the radiation field reaching the disk is completely dominated by FUV photons ($E < 13.6$ eV). The FUV radiation field incident on the ionization front of the bar is $G_0 = 2–7 \times 10^4$ in Habing units[11,49] ($G_0 = 1$ corresponds to a flux integrated between 91.2 and 240 nm of 1.6×10^{-3} erg cm^{-2} s^{-1}), as derived from UV-pumped IR-fluorescent lines[11,50]. d203-506 may be illuminated by the Trapezium cluster (Θ^1 Ori C) but also by Θ^2 Ori A[51]. The estimate of the FUV field at the surface of the disk is uncertain, but it is expected to be like that at the ionization front as determined by geometrical considerations (distance between the disk and both stars) and UV-pumped IR-fluorescent lines (O I and H_2)[48]. Moreover, H_2 rovibrational lines highlight a bright molecular emission originating from a photo-evaporative wind surrounding the edge-on disk. As seen in Fig. 1, a bright emission spot is visible in the H_2 emission in the northwestern part of the d203-506 system. This spot appears to coincide with the region of interaction between a jet and the wind. It is visible only on the side facing the Trapezium. The molecular lines (such as OH or pure rotational H_2 lines) between the bright spot and the more diffuse wind are similar in relative intensity, suggesting that the molecular excitation is primarily powered by the external FUV. However, shocks could impact the bright spot's chemistry because the collimated jet could compress the gas and increase the density locally, which would explain the brightness of the spot.

In this bright spot, we detect a very active warm-water chemistry. We can estimate two timescales to understand its origin. The chemical timescale for water chemistry is determined using the photodissociation rate of water k_Φ: $\tau_{\rm photo} = 1/k_\Phi$. This estimate leads to a chemical timescale of about a day. In comparison, the dynamical timescale of the outflowing gas $\tau_{\rm dyn}$ is much longer. It can be estimated as $\tau_{\rm dyn} = d/v_{\rm adv}$, where d is the distance between the inner disk and the bright spot and $v_{\rm adv}$ is the advection velocity. For d203-506, $d \approx 100$ au and $v_{\rm adv} \lesssim 10$ km s^{-1}, thus $\tau_{\rm dyn} \gtrsim 50$ yr.

Excitation diagram of H_2 and OH

The integrated line intensities of OH and H_2 measured with NIRSpec and MIRI-MRS are reported in Extended Data Tables 1 and 2. They were derived by fitting each line in the spectra by a Gaussian function plus a linear function to account for the continuum. We note that the H_2 line intensities toward d203-506 are also reported in ref. 52 using a slightly different aperture. The excitation diagrams of OH and H_2 are derived by plotting $Y \equiv \ln\left(\frac{4\pi I}{h\nu_0 A_{\rm ul} g_u}\right)$ as a function of the upper energy level $E_{\rm up}$ of each transition, where I is the integrated line intensity, and $A_{\rm ul}$ and ν_0 are the Einstein A coefficient and the frequency of the line, respectively. An excitation temperature $T_{\rm ex}$ and, for H_2 lines, a total column density N can then be inferred using the canonical formula:

$$Y = \ln\left(\frac{N}{Q(T_{\rm ex})}\right) - E_{\rm u}/k_{\rm B}T_{\rm ex}, \quad (1)$$

where $Q(T_{\rm ex})$ is the partition function.

The excitation diagram of the OH lines is presented in Extended Data Fig. 5 and analysed in the main text. The excitation diagram of H_2 shown in Extended Data Fig. 4 was made using the Python module called the PhotoDissociation Region Toolbox (https://github.com/mpound/pdrtpy, pdrtpy)[43–46]. The excitation of the rovibrational lines up to energy levels of ~8,000 K can be described by a single excitation temperature of ~1,000 K. This corresponds to the average gas temperature of the warm H_2 layer where OH and H_2O are efficiently formed and photodestroyed. We further infer from equation (1) a column density $N(H_2) = 9.9 \times 10^{19}$ cm^{-2}.

The OH model

Our OH model includes the rovibrational, Λ-doubling and fine structure levels of OH in its ground electronic state OH($X^2\Pi$) and in its first electronic state OH($A^2\Sigma^+$) as provided by refs. 53,54 and compiled in ref. 21. The synthetic JWST spectra for OH are calculated using the molecular excitation code GROSBETA[21] and the results of quantum dynamical calculations[19,22]. The excitation model is based on a single-zone approach following the formalism presented in ref. 55. The population of OH levels is computed by considering the production of OH in various states, radiative pumping and inelastic collisional (de-)excitation. Assuming a chemical steady state, the detailed balance equation for level i along the line of sight is given by:

$$\sum_{j\neq i} P_{ji}N_j - N_i\sum_{j\neq i} P_{ij} + F \times \left(f_i({\rm OH}) - \frac{N_i({\rm OH})}{N({\rm OH})}\right) = 0, \quad (2)$$

where N(OH) is the total column density of OH and N_i (cm^{-2}) are the column densities in level i. P_{ij} are the radiative and inelastic collisional transition probabilities. The inelastic collisional (de-)excitation of OH with He and H_2 was determined using inelastic collisional rate coefficients from refs. 56,57 and have been extrapolated to include collisional transitions between higher rotational levels of OH such as was done in ref. 21. In this work, the column density of OH is fixed at $N({\rm OH}) = 2 \times 10^{15}$ cm^{-2} and the density at $n_{\rm H} = 10^7$ cm^{-3}. We further adopt a local radiation field composed of a diluted black body at 40,000 K to model the UV radiation field emitted by the Trapezium stars, an IR radiation field corresponding to that detected by NIRSpec and MIRI-MRS, and a diluted black body at 100 K to account for the far-IR and millimetre emission from the dust. We stress that because inelastic collisional de-excitation and radiative pumping of the OH levels probed by JWST are orders of magnitude weaker than the radiative decay, the exact values of N(OH), $n_{\rm H}$ and the local radiation field are of little importance.

In equation (2), F is the formation rate, measured in cm^{-2} s^{-1}, that produces OH in specific states i with a probability denoted as f_i. We assumed that the probability of destroying OH from a state i is equal to the proportion of OH in this state N_i/N(OH) and that the other formation and destruction processes do not impact the level population. For clarity, we compute synthetic spectra including either H_2O photodissociation or chemical formation pumping. This approach is valid because these two processes excite different energy levels. Thus, we define two different formation rates: the formation rate due to the photodissociation of water denoted as Φ and the formation rate through O + H_2 denoted as R. Φ is also the column density of H_2O photodissociated per unit of time[21]:

$$\Phi \equiv \int_z k_\phi n_{\rm H_2O}\,{\rm d}z, \quad (3)$$

where $n_{\rm H_2O}$ is the local number density of H_2O (cm^{-3}) and k_ϕ is the photodissociation rate of H_2O forming OH (s^{-1}), which depends on the strength and shape of the local FUV radiation field[58]. Similarly, R is also the column density of OH formed per unit of time through O + H_2:

$$R \equiv \int_z \sum_i \sum_j k_{j\to i}(T)x_j({\rm H_2})n_{\rm H_2}n_{\rm O}\,{\rm d}z = \int_z k n_{\rm H_2}n_{\rm O}\,{\rm d}z, \quad (4)$$

where $n_{\rm O}$ and $n_{\rm H_2}$ are the number densities of atomic oxygen and molecular hydrogen, $x_j(H_2)$ is the level population of H_2, and $k_{j\to i}$ is the state-to-state rate coefficient of the reaction (cm^3 s^{-1}).

The distributions of nascent OH f_i stem from the results of quantum dynamical calculations and are shown in Extended Data Fig. 6. For H_2O photodissociation, we use the rotational and vibrational state distribution of OH produced by H_2O photodissociation through both its $\tilde{A}$ and $\tilde{B}$ electronic states calculated by refs. 19,22 and compiled by ref. 21. Since these pioneering calculations did not include the

spin–orbit coupling nor the Λ doubling, we include the results from ref. 20 by assuming that photodissociation through the $\tilde{B}$ state leads to OH in symmetric states with an equal distribution between the two spin–orbit manifolds (see Extended Data Fig. 3 for the spectroscopy of OH). The resulting state distribution of OH is calculated by integrating the state-specific cross section over a UV field represented by a black body at $T_{\rm eff}$ = 40,000 K (ref. 21). In the absence of systematic quantum dynamical calculations for short-wavelength photons, we further neglect the impact of H_2O photodissociation shortward of 114 nm on the excitation of OH.

For the formation pumping of OH, we extracted the distribution of nascent OH from the state-to-state rate coefficients computed in ref. 24. Because the distribution of OH depends on both the kinetic temperature and the population of H_2, the distributions are computed as:

$$f_i(\mathrm{OH}) = \sum_j k_{j\to i}(T) x_j(\mathrm{H_2}) / \sum_i \sum_j k_{j\to i}(T) x_j(\mathrm{H_2}), \quad (5)$$

where $x_j(H_2)$ is the level population of H_2 and $k_{j\to i}(T)$ are the state-to-state rate coefficients at temperature T. The values of $x_j(H_2)$ are inferred from the excitation diagram of H_2, which probes the majority of H_2 levels. For the $H_2(v=0, J=0)$, $H_2(v=0, J=1)$ and $H_2(v=0, J=2)$ levels, which are not probed by JWST, we extrapolated their populations assuming local thermodynamical equilibrium. Interestingly, we find that the resulting distribution of OH differs very little from a distribution assuming a Boltzmann distribution of H_2 levels at $T \simeq 1{,}000$ K. In fact, the formation rate of OH($v=1$) is driven by the rotationally excited levels $H_2(v=0, J\simeq 4\text{–}9)$, which are much more populated than the vibrational levels and are reactive enough to produce vibrationally excited OH by reacting with O atoms.

Conversion between line intensity and formation rate

In the d203-506 system, we find that the highly excited rotational and vibrational OH levels are primarily populated by formation pumping (the reaction $O + H_2$ or the photodissociation of water) followed by radiative decay, with a negligible impact of radiative pumping and inelastic collisions. Furthermore, the rovibrational and rotationally excited lines are optically thin. In the optically thin regime, the integrated line intensity is proportional to the column density of OH in the upper energy state:

$$I_{i\to j} = \frac{h\nu_{i,j}A_{i,j}}{4\pi} N_i. \quad (6)$$

Assuming that excited OH levels are populated only by formation pumping and radiative decay and that the fraction of OH in rotationally and rovibrationally excited states constitutes a negligible fraction of the total population of OH, the detailed balance equation (2) can simply be written as:

$$\sum_{j,j\neq i} M_{ji}N_j + Ff_i = 0 \quad \text{where} \quad M_{ji} = \begin{cases} A_{ji} & \text{if } i \neq j, \\ -\sum_k A_{ik} & \text{if } i = j. \end{cases} \quad (7)$$

This system of linear equations on N_i shows that N_i and, therefore, the intensity I_{ij} are simply proportional to F, the formation rate of OH. Following ref. 21, we can, therefore, define the intensity as:

$$I_{ij} = \frac{h\nu_{i,j}}{4\pi} \tilde{I}_{ij} F, \quad (8)$$

where $\tilde{I}_{ij}$ is the dimensionless proportionality factor. It corresponds to the probability that a nascent OH eventually cascades by the radiative transition $i \to j$.

$\tilde{I}_{ij}$ depends only on f_i, which in turn depends on the shape of the radiation field for excitation by H_2O photodissociation and the gas temperature and the population of H_2 for chemical formation pumping. For water photodissociation, $\tilde{I}_{ij}$ is provided in Appendix D of ref. 21 for various shapes of the UV radiation field. For the chemical pumping formation through $O + H_2 \to OH + H$, the proportionality factor computed at T = 1,000 K summed over all four components of the $v = 1 \to 0$, $N = 4 \to 5$ rovibrational lines is $\tilde{I} = 2.3 \times 10^{-2}$.

Estimating the column density of warm water and the local gas density

Our knowledge of the evolution of matter in space, from diffuse clouds to planets, depends on our ability to assess the local physical and chemical properties of the gas. Thanks to the derived value of the OH formation rates through the photodissociation of water (Φ) and through $O + H_2$ (R), one can derive astrophysical quantities such as the column density of warm water $N(H_2O)$ and the local gas density. Assuming an homogeneous medium, equation (3) can be rewritten as

$$N(\mathrm{H_2O}) = \frac{\Phi}{k_\phi}, \quad (9)$$

where the photodissociation rate k_ϕ depends on the FUV radiation field. Based on the OH mid-IR lines, we estimate $\Phi = 1.1 \times 10^{10}$ cm^{-2} s^{-1} (see main text). We can obtain an estimate of the photodissociation rate of H_2O based on the local FUV field intensity. In the d203-506 system, the exposed reservoir of water probably lies at low visual extinction. Here, we assume that the FUV field at the H^0/H_2 transition is extincted by as much as a factor 5 such that $k_\phi \simeq 1 \times 10^{-5}$ to 2×10^{-6} s^{-1} in the bright spot, corresponding to a visual extinction of $A_V \lesssim 1$. This translates to $N(H_2O) \simeq 1 \times 10^{15}$ to 5×10^{15} cm^{-2}.

Similarly, assuming a homogeneous medium, the local density can be estimated from the inferred value of R from equation (4) as:

$$n_{\rm H} = \frac{R}{kN(\mathrm{H_2})x(\mathrm{O})}, \quad (10)$$

where k is the rate coefficient of the reaction, $N(H_2)$ is the column density of H_2, $x(O)$ is the oxygen abundance and $n_{\rm H}$ is the total number density of hydrogen atoms. For d203-506, we found a column density of warm H_2 of $N(H_2) = 9.9 \times 10^{19}$ cm^{-2} and $T \simeq 1{,}000$ K from the rotational and rovibrational lines (Extended Data Fig. 4). From the estimates of the temperature and the excitation of H_2, we can derive the rate coefficient $k = 2.8 \times 10^{-13}$ cm^3 s^{-1}. Using the estimate of $R = 1.2 \times 10^{11}$ cm^{-1} s^{-1} from the OH near-IR lines and assuming $x(O) = 3 \times 10^{-4}$, we derive $n_{\rm H} = 1.4 \times 10^7$ cm^{-3}.

Rovibrational excitation of OH

In this work, we provide evidence that the near-IR OH lines are excited by chemical pumping through $O + H_2 \to OH + H$. In this section, we review alternative processes that can lead to vibrationally excited OH in the ground electronic state.

Water photodissociation through the $\tilde{A}$ electronic state by long-wavelength photons produces rotationally cold but vibrationally hot OH. Our OH model does include this process using the OH distribution computed as described in ref. 22 and also uses the improved H_2O $\tilde{A}$ state potential energy surface of ref. 59. The resulting OH emission spectrum when considering only water photodissociation through both the $\tilde{A}$ and $\tilde{B}$ states is shown in Extended Data Fig. 7. The overall shape of the modelled near-IR spectrum is very different from that observed. The rovibrational line within the $v = 1 \to 0$ band exhibits a much lower rotational temperature, and the $v = 2 \to 1$ band is predicted to be strong. Adopting the value of Φ that fits the mid-IR lines of OH, we also find that the rovibrational lines are typically a factor 10–20 weaker than the observed near-IR lines.

UV radiative pumping of OH through the A–X band can also produce vibrationally excited OH in the ground electronic state.

Our excitation model does take into account this process since the OH levels extend to the non-dissociative OH($A^2\Sigma^+$) electronic state. Discarding OH chemical pumping in the excitation model, we find that the OH near-IR spectrum is about two to three orders of magnitude weaker than observed and exhibits a too cold rotational temperature within the $v = 1$ state. Note that for UV pumping, the intensity of the lines depends on the assumed column density of OH, which is not directly probed by our observations. However, the adopted column density of $N(\mathrm{OH}) = 2 \times 10^{15}$ cm^{-2} is a good first-order estimate, since it corresponds to an OH abundance of $x(\mathrm{OH}) \simeq 10^{-5}$, a value that is in line with the results from physicochemical models[41].

Little is known about the inelastic collisional cross sections connecting the $v = 0$ and the $v = 1$ states of OH. Owing to the repulsive barrier between OH and H_2 and between OH and He, collisions with H_2 and He are negligible compared to those with atomic hydrogen, which is probably abundant in the OH-emitting layer. Collision with the latter is, thus, the only process that can contribute to the excitation of OH($v = 1$). In fact, ref. 60 computed the inelastic de-excitation collisional rate coefficients for OH($v = 1$) + H → OH($v = 0$) + H below a kinetic temperature of $T = 300$ K and assuming a thermal distribution of OH levels. In the d203-506 system, the temperature is much higher, about $T \simeq 1{,}000$ K, and the rotational levels of OH even for $v = 0$ are predicted to be subthermally populated due to the low gas density ($n_H \simeq 10^7$ cm^{-3}). Extrapolating the result of ref. 60 to the conditions in the OH-emitting gas remains uncertain. Still, for a temperature of $T \simeq 1{,}000$ K, we estimate a rate of the order of $k_{coll} \simeq 5 \times 10^{-13}$ cm^3 s^{-1}. The ratio between the OH($v = 1$) formed by chemical formation pumping and by inelastic collisions is about $x(\mathrm{OH})k_{coll}/x(\mathrm{O})k_{chem,v=1}$, where $k_{chem,v=1}$ is the formation rate for O + H_2 leading to OH($v = 1$) and where we assume $x(\mathrm{H}) \simeq x(\mathrm{H_2})$. We conclude that chemical pumping dominates over inelastic collisional excitation for an abundance ratio of about $x(\mathrm{O})/x(\mathrm{OH}) \gtrsim 10$. The calculation of inelastic collisional rate coefficients is warranted to evaluate the contribution of inelastic collisions in the emission of OH. If inelastic collisions were to contribute to the near-IR emission of OH, the inferred chemical formation rate R would be lower. However, we stress that the formation rate of O + H_2 → OH + H is close to the destruction rate of OH through photodissociation, as inferred from [O I] emission. This provides further evidence that the bulk part of OH emission is produced by chemical formation and not by inelastic collisional excitation.

Quantum dynamical calculations for O + H_2

This section summarizes the ab initio quantum determination of the state-to-state rate coefficients of the reaction O(^{3}P) + $H_2(v,j)$ → OH(v', j') + H used in our OH excitation and chemical models (see also ref. 24). Time-independent quantum-mechanical scattering calculations applied the coupled-channel hyperspherical method implemented in the ABC code[61] to yield the usual S matrix, from which the state-to-state cross sections and rate coefficients can be computed. The set of potential energy surfaces calculated by ref. 62 was used, which includes the potential energy surfaces of the two electronic states (one of symmetry ^{3}A″ and one of symmetry ^{3}A') that correlate adiabatically with the electronic ground state of reactants O(^{3}P) + H_2 and products OH($^2\Pi$) + H. Scattering calculations were carried out at 60 energies between 0.3 and 2.5 eV, including all partial waves (J) needed to reach convergence ($J_{max} = 62$) and all the values of the helicity (Ω) up to 26. Quantum-mechanical scattering calculations provided the cross section as a function of the rotational quantum number, assuming that OH is a closed-shell molecule. To calculate the nascent rotational population of OH in terms of the total angular momentum excluding the spin N, we plotted the calculated cross sections as a function of the rotational energy and assigned to the N state the cross section corresponding to the actual energy of that state. Our calculations do not distinguish between the two spin–orbit manifolds, and the procedure of ref. 63 was used to distribute the population of the product's rotational states into the two Λ-doublet components. The propagation was carried out in 300 log-derivative steps, with a maximum value of the hyperradius of $20a_0$. The basis included all the diatomic energy levels up to 3.25 eV.

Since reactions can occur on both ^{3}A' and ^{3}A″ electronic states, the total rate constant of the reaction is obtained as a weighted average of the respective rates $k_{A'}$ and $k_{A''}$. The weights are obtained by establishing the correlation between the electronic states A' and A″ and the spin–orbit levels of oxygen and are, thus, related to their relative population. It is found that the 1^3A″ state correlates with three of the five components of O($^3P_2$) whereas the 1^3A' state correlates with the other two components of O($^3P_2$) and one component of O($^3P_1$). Under these considerations and assuming a thermal distribution of the spin–orbit levels of the oxygen atom, the overall thermal rate coefficients are calculated as in ref. 24:

$$k(T) = \frac{3k_{A''}(T) + [2 + \exp(-\Delta E_1/T)]\,k_{A'}(T)}{5 + 3\exp(-\Delta E_1/T) + \exp(-\Delta E_0/T)}, \quad (11)$$

where $k(T)$ refer to the desired (v,j → v',j') state-to-state rate coefficient at a given temperature, and $k_{A'}(T)$ and $k_{A''}(T)$ are the state-to-state rate coefficients on the A' and A″ potential energy surfaces, respectively. $\Delta E_1 = 227.708$ K and $\Delta E_0 = 326.569$ K are the energies of the oxygen atom spin–orbit levels $^3P_1$ and $^3P_0$, respectively, over the ground state $^3P_2$. Note that the $^3P_0$ contribution and two contributions of $^3P_1$ do not appear in the numerator because these spin–orbit states are not reactive and will not contribute to the total rate constants of OH formation.

Data availability

The JWST data presented in this paper are publicly available through the MAST online archive (http://mast.stsci.edu) using the PID 1288. The MIRI-MRS and NIRSpec spectra presented in Figs. 2 and 3 and Extended Data Fig. 8 are available in ASCII format at https://doi.org/10.5281/zenodo.10634184.

Code availability

The JWST pipeline used to produce the final data products presented in this article is available at https://github.com/spacetelescope/jwst. The GROSBETA code used in this study is available from the corresponding author on reasonable request.

References

1. van Dishoeck, E. F. et al. Water in star-forming regions: physics and chemistry from clouds to disks as probed by Herschel spectroscopy. *Astron. Astrophys.* **648**, A24 (2021).
2. Glassgold, A. E., Meijerink, R. & Najita, J. R. Formation of water in the warm atmospheres of protoplanetary disks. *Astrophys. J.* **701**, 142–153 (2009).
3. Bethell, T. & Bergin, E. Formation and survival of water vapor in the terrestrial planet-forming region. *Science* **326**, 1675 (2009).
4. Thi, W. F., Woitke, P. & Kamp, I. Warm non-equilibrium gas phase chemistry as a possible origin of high HDO/H_2O ratios in hot and dense gases: application to inner protoplanetary discs. *Mon. Not. R. Astron. Soc.* **407**, 232–246 (2010).
5. Salyk, C., Pontoppidan, K. M., Blake, G. A., Najita, J. R. & Carr, J. S. A Spitzer survey of mid-infrared molecular emission from protoplanetary disks. II. Correlations and local thermal equilibrium models. *Astrophys. J.* **731**, 130 (2011).
6. Carr, J. S. & Najita, J. R. Organic molecules and water in the inner disks of T Tauri stars. *Astrophys. J.* **733**, 102 (2011).
7. Pontoppidan, K. M. et al. in *Protostars and Planets VI* (eds Beuther, H. et al.) 363–385 (Univ. Arizona Press, 2014).
8. Mandell, A. M. et al. First detection of near-infrared line emission from organics in young circumstellar disks. *Astrophys. J.* **747**, 92 (2012).

9. Berné, O. et al. PDRs4All: a JWST early release science program on radiative feedback from massive stars. *Publ. Astron. Soc. Pac.* **134**, 054301 (2022).
10. Tielens, A. G. G. M. et al. Anatomy of the photodissociation region in the Orion bar. *Science* **262**, 86–89 (1993).
11. Peeters, E. et al. PDRs4All III: JWST's NIR spectroscopic view of the Orion bar. Preprint at https://arXiv.org/abs/2310.08720 (2023).
12. Adams, F. C. The birth environment of the Solar System. *Annu. Rev. Astron. Astrophys.* **48**, 47–85 (2010).
13. Winter, A. J. & Haworth, T. J. The external photoevaporation of planet-forming discs. *Eur. Phys. J. Plus* **137**, 1132 (2022).
14. Tabone, B., Raga, A., Cabrit, S. & Pineau des Forêts, G. Interaction between a pulsating jet and a surrounding disk wind. A hydrodynamical perspective. *Astron. Astrophys.* **614**, A119 (2018).
15. Tappe, A., Lada, C. J., Black, J. H. & Muench, A. A. Discovery of superthermal hydroxyl (OH) in the HH 211 outflow. *Astrophys. J. Lett.* **680**, L117 (2008).
16. Najita, J. R. et al. Spitzer spectroscopy of the transition object TW Hya. *Astrophys. J.* **712**, 274–286 (2010).
17. Carr, J. S. & Najita, J. R. The OH rotational population and photodissociation of H_2O in DG Tauri. *Astrophys. J.* **788**, 66 (2014).
18. Harich, S. A., Yang, X., Yang, X. & Dixon, R. N. Extremely rotationally excited OH from water (HOD) photodissociation through conical intersection. *Phys. Rev. Lett.* **87**, 253201 (2001).
19. van Harrevelt, R. & van Hemert, M. C. Photodissociation of water. II. Wave packet calculations for the photofragmentation of H_2O and D_2O in the $\tilde{B}$ band. *J. Comp. Phys.* **112**, 5787–5808 (2000).
20. Zhou, L., Xie, D. & Guo, H. Signatures of non-adiabatic dynamics in the fine-structure state distributions of the OH($\tilde{X}/\tilde{A}$) products in the B-band photodissociation of H_2O. *J. Comp. Phys.* **142**, 124317 (2015).
21. Tabone, B., van Hemert, M. C., van Dishoeck, E. F. & Black, J. H. OH mid-infrared emission as a diagnostic of H_2O UV photodissociation. I. Model and application to the HH 211 shock. *Astron. Astrophys.* **650**, A192 (2021).
22. van Harrevelt, R. & van Hemert, M. C. Photodissociation of water in the $\tilde{A}$ band revisited with new potential energy surfaces. *J. Chem. Phys.* **114**, 9453–9462 (2001).
23. Weck, P. F., Balakrishnan, N., Brandão, J., Rosa, C. & Wang, W. F. Dynamics of the O(3*P*)+H_2 reaction at low temperatures: comparison of quasiclassical trajectory with quantum scattering calculations. *J. Chem. Phys.* **124**, 74308 (2006).
24. Veselinova, A. et al. Quantum study of reaction $O(^3P)+H_2(v,j)\rightarrow OH+H$: OH formation in strongly UV-irradiated gas. *Astron. Astrophys.* **648**, A76 (2021).
25. Goicoechea, J. R. et al. OH emission from warm and dense gas in the Orion bar PDR. *Astron. Astrophys.* **530**, L16 (2011).
26. Menten, K. M., Reid, M. J., Forbrich, J. & Brunthaler, A. The distance to the Orion nebula. *Astron. Astrophys.* **474**, 515–520 (2007).
27. Bosman, A. D., Bergin, E. A., Calahan, J. & Duval, S. E. Water UV-shielding in the terrestrial planet-forming zone: implications from water emission. *Astrophys. J. Lett.* **930**, L26 (2022).
28. Bally, J., O'Dell, C. R. & McCaughrean, M. J. Disks, microjets, windblown bubbles, and outflows in the Orion nebula. *Astron. J.* **119**, 2919–2959 (2000).
29. Störzer, H. & Hollenbach, D. On the [O I] λ6300 line emission from the photoevaporating circumstellar disks in the Orion nebula. *Astrophys. J. Lett.* **502**, L71–L74 (1998).
30. van Dishoeck, E. F. & Dalgarno, A. Photodissociation of OH in interstellar clouds. *Astrophys. J.* **277**, 576 (1984).
31. Hagemann, R., Nief, G. & Roth, E. Absolute isotopic scale for deuterium analysis of natural waters. Absolute D/H ratio for SMOW. *Tellus* **22**, 712–715 (1970).
32. Prodanović, T., Steigman, G. & Fields, B. D. The deuterium abundance in the local interstellar medium. *Mon. Not. R. Astron. Soc.* **406**, 1108–1115 (2010).
33. Cleeves, L. I. et al. The ancient heritage of water ice in the Solar System. *Science* **345**, 1590–1593 (2014).
34. Tielens, A. G. G. M. Surface chemistry of deuterated molecules. *Astron. Astrophys.* **119**, 177–184 (1983).
35. Ceccarelli, C. et al. in *Protostars and Planets VI* (eds Beuther, H. et al.) 859–882 (Univ. Arizona Press, 2014).
36. Persson, M. V., Jørgensen, J. K., van Dishoeck, E. F. & Harsono, D. The deuterium fractionation of water on Solar-System scales in deeply-embedded low-mass protostars. *Astron. Astrophys.* **563**, A74 (2014).
37. Jensen, S. S. et al. ALMA observations of doubly deuterated water: inheritance of water from the prestellar environment. *Astron. Astrophys.* **650**, A172 (2021).
38. Tobin, J. J. et al. Deuterium-enriched water ties planet-forming disks to comets and protostars. *Nature* **615**, 227–230 (2023).
39. Le Petit, F., Roueff, E. & Le Bourlot, J. D/HD transition in photon dominated regions (PDR). *Astron. Astrophys.* **390**, 369–381 (2002).
40. Ballabio, G., Haworth, T. J. & Henney, W. J. [O I] 6300 Å emission as a probe of external photoevaporation of protoplanetary discs. *Mon. Not. R. Astron. Soc.* **518**, 5563–5575 (2023).
41. Zannese, M. et al. OH mid-infrared emission as a diagnostic of H_2O UV photodissociation—II. Application to interstellar photodissociation regions. *Astron. Astrophys.* **671**, A41 (2023).
42. Neufeld, D. A. et al. Observations and analysis of CH^+ vibrational emissions from the young, carbon-rich planetary nebula NGC 7027: a textbook example of chemical pumping. *Astrophys. J.* **917**, 15 (2021).
43. Pound, M. W. & Wolfire, M. G. The photo dissociation region toolbox: software and models for astrophysical analysis. *Astron. J.* **165**, 25 (2023).
44. Pound, M. W. & Wolfire, M. G. The photo dissociation region toolbox. In *Astronomical Data Analysis Software and Systems XVII* Vol. 394 (eds Argyle, R. W. et al.) 654 (Astronomical Society of the Pacific Conference Series, 2008).
45. Kaufman, M. J., Wolfire, M. G. & Hollenbach, D. J. [Si II], [Fe II], [C II], and H_2 emission from massive star-forming regions. *Astrophys. J.* **644**, 283–299 (2006).
46. Pound, M. W. & Wolfire, M. G. PDRT: Photo Dissociation Region Toolbox. *Astrophysics Source Code Library* ascl:1102.022 (2011).
47. Chown, R. et al. PDRs4All IV. An embarrassment of riches: aromatic infrared bands in the Orion bar. *Astron. Astrophys.* https://doi.org/10.1051/0004-6361/202346662 (2024).
48. Berné, O. et al. A far-ultraviolet-driven photoevaporation flow observed in a protoplanetary disk. *Science* https://doi.org/10.1126/science.adh2861 (2024).
49. Habing, H. J. The interstellar radiation density between 912 A and 2400 A. *Bull. Astron. Inst. Neth.* **19**, 421 (1968).
50. Marconi, A., Testi, L., Natta, A. & Walmsley, C. M. Near infrared spectra of the Orion bar. *Astron. Astrophys.* **330**, 696–710 (1998).
51. Haworth, T. J. et al. The VLT MUSE NFM view of outflows and externally photoevaporating discs near the Orion bar. *Mon. Not. R. Astron. Soc.* **525**, 4129–4142 (2023).
52. Berné, O. et al. Formation of the methyl cation by photochemistry in a protoplanetary disk. *Nature* **621**, 56–59 (2023).
53. Brooke, J. S. A. et al. Line strengths of rovibrational and rotational transitions in the $X^2\Pi$ ground state of OH. *J. Quant. Spectrosc. Radiat. Transf.* **168**, 142–157 (2016).
54. Yousefi, M., Bernath, P. F., Hodges, J. & Masseron, T. A new line list for the $A^2\Sigma+–X^2\Pi$ electronic transition of OH. *J. Quant. Spectrosc. Radiat. Transf.* **217**, 416–424 (2018).
55. Van Der Tak, F. F. S., Black, J. H., Schöier, F. L., Jansen, D. J. & Van Dishoeck, E. F. A computer program for fast non-LTE analysis of interstellar line spectra. *Astron. Astrophys.* **468**, 627–635 (2007).

56. Kłos, J., Lique, F. & Alexander, M. H. Temperature dependence of rotational excitation rate coefficients of OH($X^2\Pi$) in collision with He. *Chem. Phys. Lett.* **445**, 12–16 (2007).
57. Offer, A. R., van Hemert, M. C. & van Dishoeck, E. F. Rotationally inelastic and hyperfine resolved cross sections for OH–H_2 collisions. Calculations using a new ab initio potential surface. *J. Comp. Phys* **100**, 362–378 (1994).
58. Heays, A. N., Bosman, A. D. & van Dishoeck, E. F. Photodissociation and photoionisation of atoms and molecules of astrophysical interest. *Astron. Astrophys.* **602**, A105 (2017).
59. van Harrevelt, R. & van Hemert, M. C. Photodissociation of water. I. Electronic structure calculations for the excited states. *J. Comp. Phys.* **112**, 5777–5786 (2000).
60. Atahan, S. & Alexander, M. H. Coupled-states statistical investigation of vibrational and rotational relaxation of OH(2Π) by collisions with atomic hydrogen. *J. Phys. Chem. A* **110**, 5436–5445 (2006).
61. Skouteris, D., Castillo, J. F. & Manolopoulos, D. E. ABC: a quantum reactive scattering program. *Comp. Phys. Commun.* **133**, 128–135 (2000).
62. Zanchet, A., Menendez, M., Jambrina, P. G. & Aoiz, F. J. New global potential energy surfaces of the ground $^3A'$ and $^3A''$ states of the O(^3P) + H_2 system. *J. Chem. Phys.* **151,** 094307 (2019).
63. Jambrina, P. G., Zanchet, A., Aldegunde, J., Brouard, M. & Aoiz, F. J. Product lambda-doublet ratios as an imprint of chemical reaction mechanism. *Nat. Commun.* **7**, 13439 (2016).
64. Faure, A. & Josselin, E. Collisional excitation of water in warm astrophysical media. I. Rate coefficients for rovibrationally excited states. *Astron. Astrophys.* **492**, 257–264 (2008).
65. Schöier, F. L., van der Tak, F. F. S., van Dishoeck, E. F. & Black, J. H. An atomic and molecular database for analysis of submillimetre line observations. *Astron. Astrophys.* **432**, 369–379 (2005).
66. Changala, P. B. et al. Astronomical CH_3^+ rovibrational assignments—a combined theoretical and experimental study validating observational findings in the d203-506 UV-irradiated protoplanetary disk. *Astron. Astrophys.* **680**, A19 (2023).

Acknowledgements

This work is based (in part) on observations made with the NASA/ESA/CSA JWST. The data were obtained from the Mikulski Archive for Space Telescopes at the Space Telescope Science Institute, which is operated by the Association of Universities for Research in Astronomy, Inc., under NASA contract NAS 5-03127 for JWST. These observations are associated with programme ERS1288. This work was supported by the French National Centre for Space Studies (CNES) with funds focused on JWST. This research has been supported by the Programme National Physique et Chimie du Milieu Interstellaire of the French National Centre for Scientific Research and the French National Institute for Earth Sciences and Astronomy with INC (Institut de Chimie)/INP (Institut de Physique) co-funded by the French Alternative Energies and Atomic Energy Commission and CNES. J.R.G. thanks the Spanish Ministry of Science, Innovation and Universities (MCINN) for funding support (Grant No. PID2019-106110GB-I00). A.Z. acknowledges funding from Grant Nos. PID2019-107115GB-C21 and PID2021-122549NB-C21. E.v.D. acknowledges support from the European Research Council (Advanced Grant No. 101019751 MOLDISK). E.V., M.M., L.G.S. and F.J.A. acknowledge funding from MCINN (Grant No. PID2021-122839NB-I00). L.G.S., P.G.J. and A.V. acknowledge funding from MCINN (Grant No. PID2020-113147GA-I00). A.V. also acknowledges support from the Junta Castilla y León and European Social Fund (Grant No. EDU/1508/2020). This work is sponsored (in part) by the Chinese Academy of Sciences (CAS), through a grant to the CAS South America Center for Astronomy in Santiago, Chile. D.v.d.P. acknowledges support for programme 1288 provided by NASA through a grant from the Space Telescope Science Institute. C.B. is grateful for an appointment at NASA Ames Research Center through the San José State University Research Foundation (Grant No. 80NSSC22M0107) and acknowledges support from the Internal Scientist Funding Model of the Laboratory Astrophysics Directed Work Package at NASA Ames. A.F. is grateful to MCINN for funding (Grant No. PID2019-106235GB-I00) and to the European Research Council for funding (Advanced Grant Project SUL4LIFE, Grant Agreement No. 101096293). Work by Y.O. and M. Röllig is carried out within the Collaborative Research Centre 956, subproject C1, funded by the German Research Foundation (Project ID 184018867). E.P. and J.C. acknowledge support from the University of Western Ontario, the Institute for Earth and Space Exploration, CSA and the Natural Sciences and Engineering Research Council of Canada. T.O. acknowledges support from a bilateral programme of the Japan Society for the Promotion of Science (Grant No. 120219939). This research made use of pdrtpy, the PhotoDissociation Region Toolbox, an open-source model for photodissociation regions and a data analysis package[43–46].

Author contributions

M.Z., B. Tabone, E.H. and A.Z. wrote the paper with input from J.R.G., E.v.D., A.T., E.B. and J.H. M.Z. and B. Tabone did the line analysis with support from A.Z. and J.H.B. using the quantum dynamical calculations of M.C.v.H., A.V., P.G.J., M.M., E.V., F.J.A. and L.G.S. I.S., A.C., R.C., A.S., B. Trahin, F.A. and D.V.P. reduced the data. E.H., E.P. and O.B. planned and co-led the ERS PDRs4All programme. B. Tabone, J.R.G., A.T., B. Trahin, E.D., A.A., F.A., E.B., J.B.S., C.B., E.A.B., J.C., A.C., R.C., D.D., M.E., A.F., K.D.G., L.I., C.J., O.K., B.K., D.L., R.L.G., A.M., R.M., Y.O., T.O., S.P., M.W.P., M. Robberto, M. Röllig, B.S., T.S., I.S., A.S., D.v.d.P., S.V. and M.G.W. contributed to the observing programme with JWST. All authors participated in the development and testing of the MIRI-MRS or NIRSpec instruments and their data reduction, participated in discussing the results or commented on the paper.

Competing interests

The authors declare no competing interests.

Additional information

Extended data Extended data are available for this paper at https://doi.org/10.1038/s41550-024-02203-0.

Correspondence and requests for materials should be addressed to Marion Zannese.

Peer review information *Nature Astronomy* thanks Jenny Calahan and Thomas Haworth for their contribution to the peer review of this work.

Reprints and permissions information is available at www.nature.com/reprints.

Publisher's note Springer Nature remains neutral with regard to jurisdictional claims in published maps and institutional affiliations.

Marion Zannese[1] ✉, Benoît Tabone[1], Emilie Habart[1], Javier R. Goicoechea[2], Alexandre Zanchet[2], Ewine F. van Dishoeck[3,4], Marc C. van Hemert[5], John H. Black[6], Alexander G. G. M. Tielens[3,7], A. Veselinova[8], P. G. Jambrina[8], M. Menendez[9], E. Verdasco[9], F. J. Aoiz[9], L. Gonzalez-Sanchez[8], Boris Trahin[1], Emmanuel Dartois[10], Olivier Berné[11], Els Peeters[12,13,14], Jinhua He[15,16,17], Ameek Sidhu[12,13], Ryan Chown[12,13], Ilane Schroetter[11], Dries Van De Putte[18], Amélie Canin[11], Felipe Alarcón[19], Alain Abergel[1], Edwin A. Bergin[19], Jeronimo Bernard-Salas[20,21], Christiaan Boersma[22], Emeric Bron[23], Jan Cami[12,13,14], Daniel Dicken[24], Meriem Elyajouri[1], Asunción Fuente[25], Karl D. Gordon[18,26], Lina Issa[11], Christine Joblin[11], Olga Kannavou[1], Baria Khan[12], David Languignon[23], Romane Le Gal[27,28], Alexandros Maragkoudakis[22], Raphael Meshaka[1,23], Yoko Okada[29], Takashi Onaka[30,31], Sofia Pasquini[12], Marc W. Pound[19], Massimo Robberto[18,32], Markus Röllig[29,33,34], Bethany Schefter[12,13], Thiébaut Schirmer[1,6], Sílvia Vicente[35] & Mark G. Wolfire[7]

[1]Université Paris-Saclay, CNRS, Institut d'Astrophysique Spatiale, Orsay, France. [2]Instituto de Física Fundamental (CSIC), Madrid, Spain. [3]Leiden Observatory, Leiden University, Leiden, The Netherlands. [4]Max-Planck Institut für Extraterrestrische Physik (MPE), Garching, Germany. [5]Leiden Institute of Chemistry, Gorlaeus Laboratories, Leiden University, Leiden, The Netherlands. [6]Department of Space, Earth and Environment, Chalmers University of Technology, Onsala Space Observatory, Onsala, Sweden. [7]Astronomy Department, University of Maryland, College Park, MD, USA. [8]Departamento de Química Física, University of Salamanca, Salamanca, Spain. [9]Departamento de Química Física (Unidad Asociada al CSIC), Universidad Complutense de Madrid, Ciudad Universitaria, Madrid, Spain. [10]Institut des Sciences Moléculaires d'Orsay, CNRS, Université Paris-Saclay, Orsay, France. [11]Institut de Recherche en Astrophysique et Planétologie, Université Toulouse III - Paul Sabatier, CNRS, CNES, Toulouse, France. [12]Department of Physics and Astronomy, University of Western Ontario, London, Ontario, Canada. [13]Institute for Earth and Space Exploration, University of Western Ontario, London, Ontario, Canada. [14]Carl Sagan Center, SETI Institute, Mountain View, CA, USA. [15]Yunnan Observatories, Chinese Academy of Sciences, Kunming, China. [16]Chinese Academy of Sciences South America Center for Astronomy, National Astronomical Observatories, CAS, Beijing, China. [17]Departamento de Astronomica, Universidad de Chile, Santiago, Chile. [18]Space Telescope Science Institute, Baltimore, MD, USA. [19]Department of Astronomy, University of Michigan, Ann Arbor, MI, USA. [20]ACRI-ST, Centre d'Etudes et de Recherche de Grasse (CERGA), Grasse, France. [21]INCLASS Common Laboratory, Grasse, France. [22]NASA Ames Research Center, Moffett Field, CA, USA. [23]LERMA, Observatoire de Paris, PSL Research University, CNRS, Sorbonne Universités, Meudon, France. [24]UK Astronomy Technology Centre, Royal Observatory Edinburgh, Edinburgh, UK. [25]Centro de Astrobiología, CAB, CSIC-INTA, Madrid, Spain. [26]Sterrenkundig Observatorium, Universiteit Gent, Gent, Belgium. [27]Institut de Planétologie et d'Astrophysique de Grenoble (IPAG), Université Grenoble Alpes, CNRS, Grenoble, France. [28]Institut de Radioastronomie Millimétrique (IRAM), Saint-Martin d'Hères, France. [29]I. Physikalisches Institut der Universität zu Köln, Cologne, Germany. [30]Department of Astronomy, Graduate School of Science, University of Tokyo, Tokyo, Japan. [31]Department of Physics, Faculty of Science and Engineering, Meisei University, Tokyo, Japan. [32]Johns Hopkins University, Baltimore, MD, USA. [33]Physikalischer Verein - Gesellschaft für Bildung und Wissenschaft, Frankfurt, Germany. [34]Institut für Angewandte Physik, Frankfurt, Germany. [35]Instituto de Astrofísica e Ciências do Espaço, Lisbon, Portugal. ✉e-mail: marion.zannese@universite-paris-saclay.fr

https://doi.org/10.1038/s41550-024-02203-0

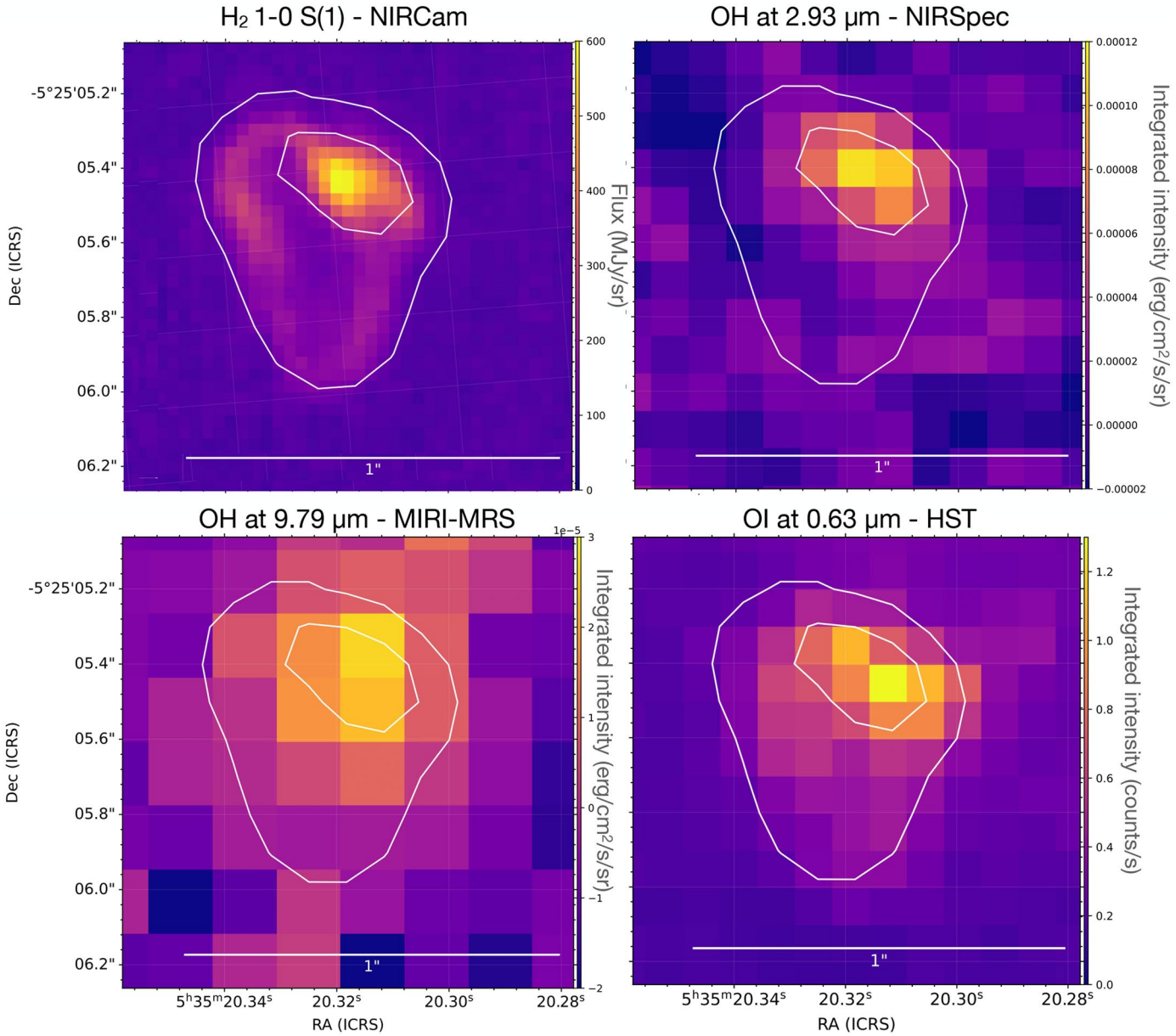

Extended Data Fig. 1 | Spatial distribution of the emission of key lines. (Top Left) d203-506 image from the NIRCam F212N filter (in MJy sr^{-1}), (Top Right) NIRSpec integrated intensity map of the OH line at 2.934 μm (in erg $cm^{-2}s^{-1}sr^{-1}$), (Bottom Left) MIRI-MRS integrated intensity map of the OH line at 9.791 μm (in erg $cm^{-2}s^{-1}sr^{-1}$), (Bottom Right) integrated intensity map of the [OI] line at 0.63 μm obtained from the Hubble Space Telescope (HST) (in counts s^{-1})[28]. The NIRSpec H_2 1-0 S(1) intensity map is shown in white contours (at 7×10^{-4}, 2×10^{-3} erg $cm^{-2}s^{-1}sr^{-1}$).

https://doi.org/10.1038/s41550-024-02203-0

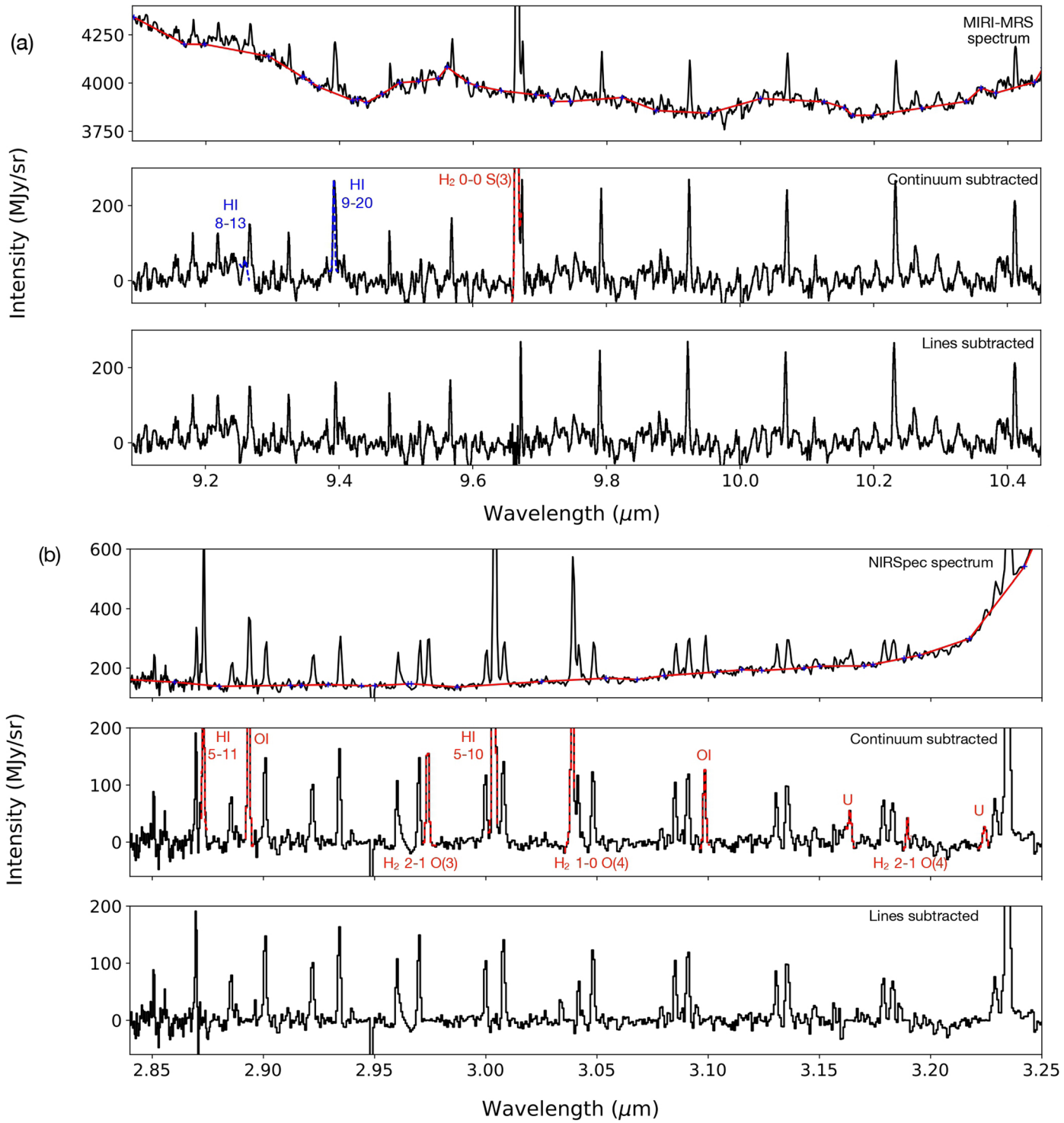

Extended Data Fig. 2 | Processing steps of the MIRI-MRS and NIRSpec spectra to better visualize the OH lines. (a) (Top panel) Spectrum observed with MIRI-MRS. The red line is the estimated continuum. (Middle panel) Continuum subtracted spectrum. The red Gaussians are the fits to lines other than OH. The blue Gaussians are the fits to lines from the OFF position which contaminate OH lines. (Bottom panel) Processed spectrum with the dust continuum and the bright lines other than OH subtracted. (b) (Top panel) Spectrum observed with NIRSpec. The red line is the estimated continuum. (Middle panel) Continuum subtracted spectrum. The red Gaussians are fits to lines other than OH. (Bottom panel) Processed spectrum with the dust continuum and the bright lines other than OH subtracted.

https://doi.org/10.1038/s41550-024-02203-0

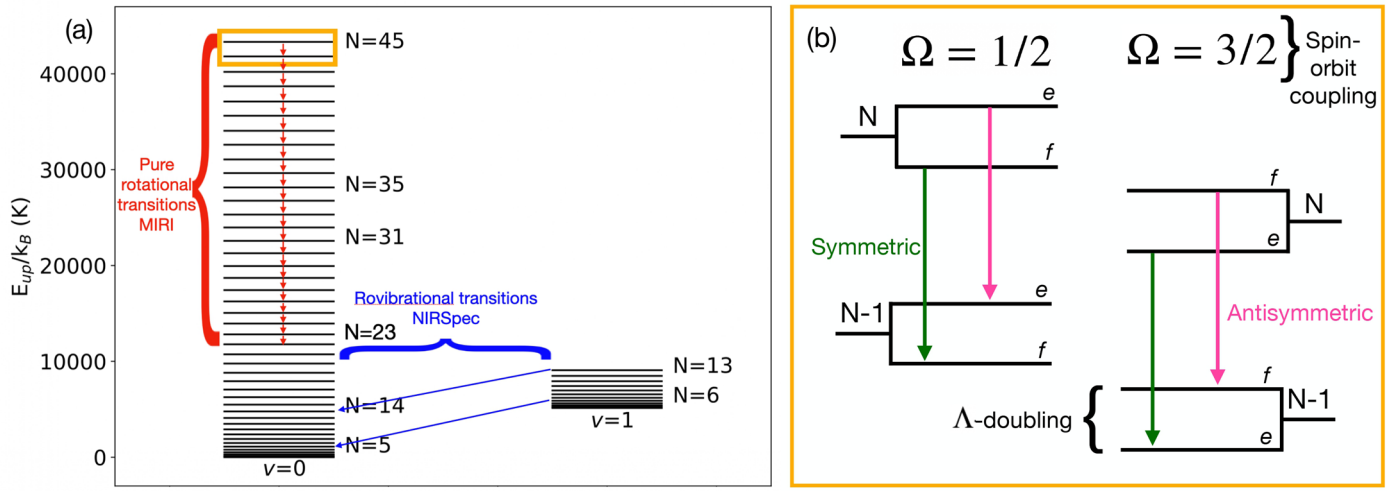

Extended Data Fig. 3 | Schematic view of OH spectroscopy relevant to JWST. (a) OH rotational and ro-vibrational energy levels. The red arrows are the pure rotational transitions observable with MIRI-MRS. The blue arrows are some of the ro-vibrational transitions observable with NIRSpec. (b) Zoom-in on the yellow box to reveal the splitting of a rotational level due to the spin-orbit coupling and the Λ-doubling. The two spin-orbit states are labeled by the Ω quantum number and the Λ-doubling states are labeled by their ϵ = e / f spectroscopic parity. The green and pink arrows are the transitions detected in the observations forming a quadruplet. The green arrows are the transitions arising from symmetric states and the pink arrows are the transitions arising from antisymmetric states.

https://doi.org/10.1038/s41550-024-02203-0

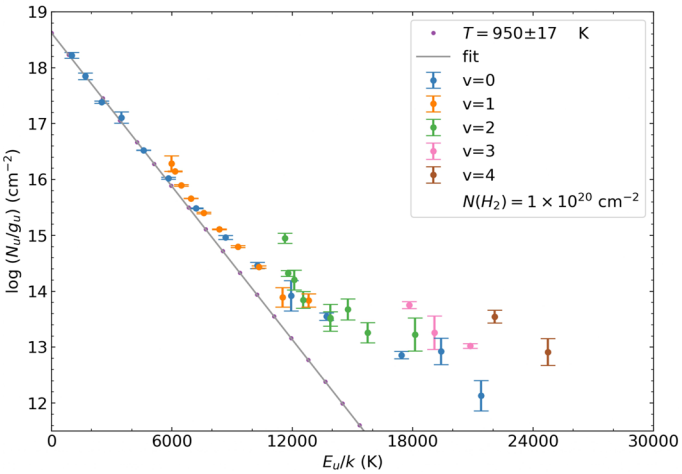

Extended Data Fig. 4 | Excitation diagram of H_2 at the bright spot. The temperature fit was made on the first five pure rotational lines. The measured line fluxes are reported in Extended Data Table 2. The uncertainties are calculated by the Python routine curve_fit as 1σ errors on the parameters. The impact of calibration effects is not taken into account and the associated uncertainties can be as high as 20%.

https://doi.org/10.1038/s41550-024-02203-0

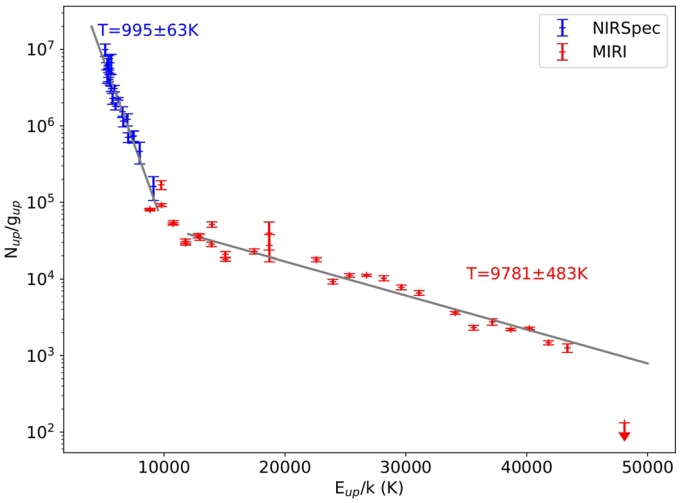

Extended Data Fig. 5 | Excitation diagram of ro-vibrational and pure rotational lines of OH. The blue crosses are the ro-vibrational transitions detected with NIRSpec (v=1-0) and the red crosses are the pure rotational transitions detected with MIRI-MRS (v=0-0). The measured line fluxes are reported in Extended Data Table 1. The uncertainties are calculated by the Python routine curve_fit as 1σ errors on the parameters. The impact of calibration effects is not taken into account and the associated uncertainties can be as high as 20%.

https://doi.org/10.1038/s41550-024-02203-0

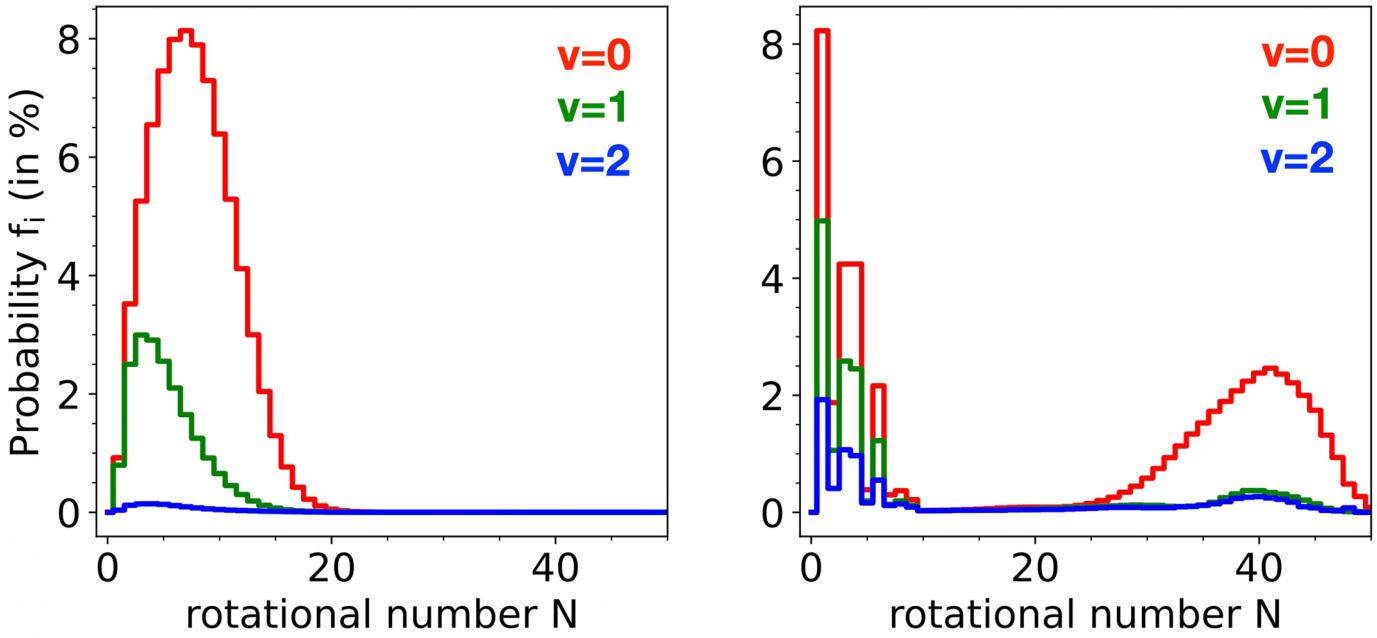

Extended Data Fig. 6 | State distributions of nascent OH predicted by quantum dynamical calculations summed over the spin-orbit and Λ-doubling states. (Left) Distribution of nascent OH following its formation via O+H_2 at a temperature of $T = 1,000$ K and for a H_2 population as inferred for d203-506. (Right) Distribution of nascent OH following H_2O photodissociation by a FUV field representative of the Orion Bar. Photodissociation by short wavelength photons λ<144 nm via the $\tilde{B}$ electronic state of water produces rotationally hot OH with rotational quantum numbers of $N \simeq 35-45$ and photodissociation by longer wavelength photons via the $\tilde{A}$ electronic state leads to rotationally cold but vibrationally hot OH.

https://doi.org/10.1038/s41550-024-02203-0

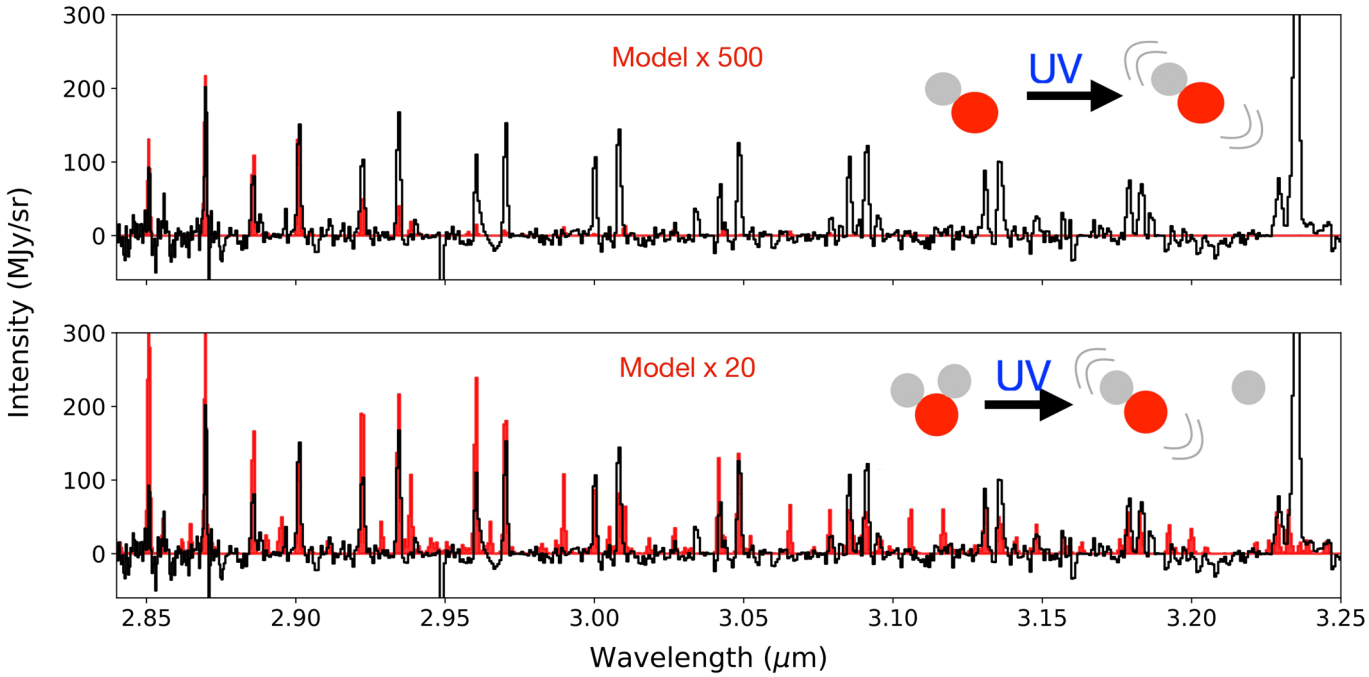

Extended Data Fig. 7 | Comparison between the observed OH near-IR emission and modeling of excitation processes other than formation-pumping. OH near-IR synthetic GROSBETA models for (Top) UV radiative pumping and (Bottom) H_2O photodissociation via its $\tilde{A}$ electronic state. None of these processes can account for the shape and strength of the observed OH ro-vibrational spectrum.

https://doi.org/10.1038/s41550-024-02203-0

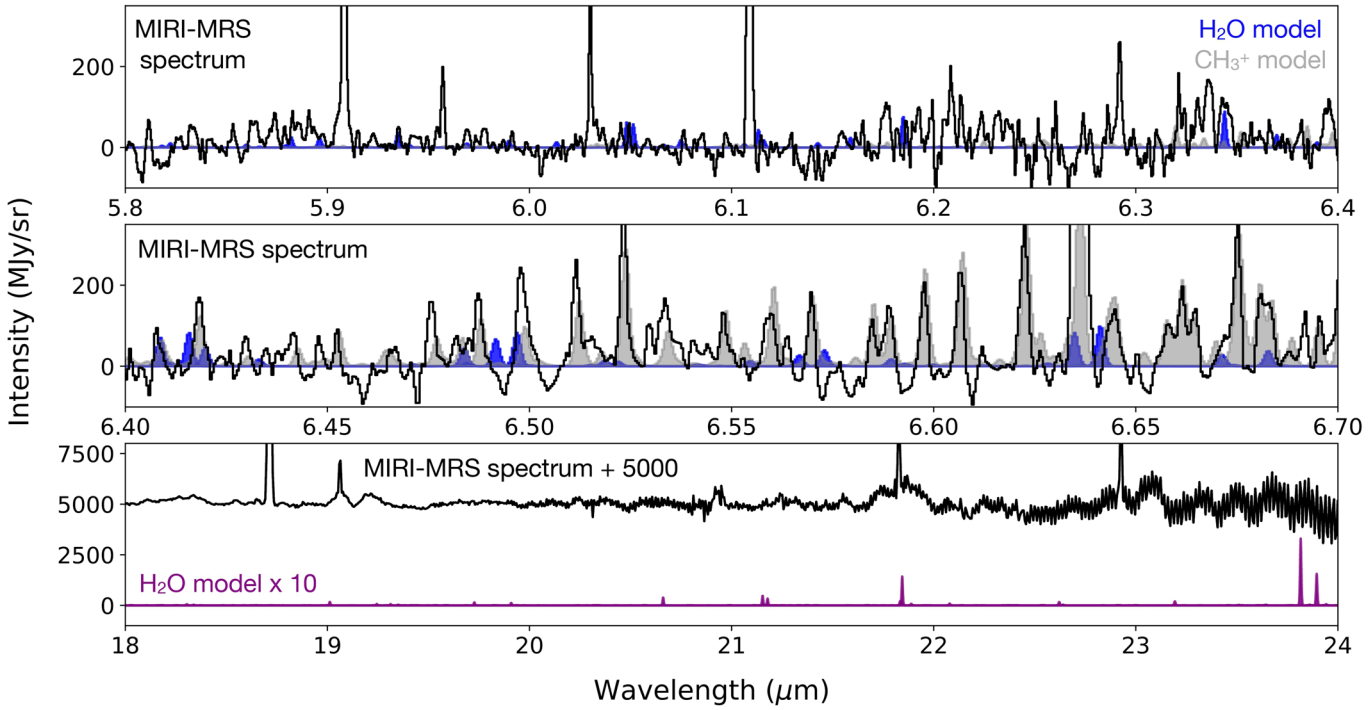

Extended Data Fig. 8 | MIRI-MRS observations versus a synthetic RADEX spectrum of the brightest H_2O lines. MIRI-MRS observations versus a synthetic RADEX[55] spectrum of the brightest H_2O lines adopting the maximum amount of unseen water of $N(H_2O) = 5 \times 10^{15} cm^{-2}$ as inferred from the mid-IR lines of OH, a temperature of T=1000K as inferred from H_2 lines and a density of $n_H = 10^7$ cm^{-3} as inferred from the near-IR lines of OH. Inelastic collisional rate coefficients are from ref. 64 and are available on the LAMDA database[65]. We also assumed an IR background inferred from NIRSpec and MIRI-MRS observations. When calculating the line intensities, we assumed that the IR continuum background interacting with the gas is not along the same line of sight as the observations as described in ref. 21. The latter assumption provides a strict upper limit on the line strength. Owing to the low gas density, H_2O is subthermally excited, leading to undetectable lines. In the 5-7 μm region, the MIRI-MRS spectrum is affected by residual fringe and possible contamination by CH_3^+[52]. An LTE model at T = 700K of CH_3^+ is overlayed in grey[66] for reference. In the 18-24 μm, the residual fringe increases due to the increase in the continuum, making the detection of H_2O lines in this region impossible. The same model of H_2O multiplied by a factor of 10 is overlayed in purple.

https://doi.org/10.1038/s41550-024-02203-0

Extended Data Table 1 | Intensities of the OH lines detected at the bright spot with MIRI-MRS and NIRSpec

MIRI-MRS

λ (μm)	N	E_{up}/k_B (K)	I ($\times 10^{-5}$ erg cm^{-2} s^{-1} sr^{-1})
9.181	44	43,343	0.91 ± 0.12
9.219	43	41,776	1.02 ± 0.07
9.266	42	40,216	1.50 ± 0.06
9.325	41	38,663	1.38 ± 0.05
9.394	40	37,120	1.64 ± 0.16
9.475	39	35,588	1.30 ± 0.09
9.568	38	34,070	1.89 ± 0.08
9.791	36	31,079	2.97 ± 0.21
9.923	35	29,609	3.24 ± 0.23
10.069	34	28,160	3.89 ± 0.30
10.232	33	26,731	3.86 ± 0.12
10.411	32	25,325	3.48 ± 0.18
10.608	31	23,943	2.58 ± 0.18
10.825	30	22,586	4.44 ± 0.27
11.610	27	18,671	3.38 ± 1.35
11.615	27	18,701	2.24 ± 0.87
11.929	26	17,447	3.30 ± 0.26
12.657	24	15,053	1.12 ± 0.10
12.665	24	15,085	0.92 ± 0.05
13.081	23	13,916	1.27 ± 0.09
13.089	23	13,949	2.20 ± 0.18
13.550	22	12,816	1.36 ± 0.09
13.560	22	12,850	1.24 ± 0.12
14.070	21	11,754	0.94 ± 0.07
14.082	21	11,789	0.84 ± 0.04
14.648	20	10,783	1.29 ± 0.04
14.664	20	10,767	1.27 ± 0.07
15.295	19	9,749	3.34 ± 0.44
15.314	19	9,786	1.71 ± 0.08
16.021	18	8,809	1.26 ± 0.03
16.045	18	8,847	1.16 ± 0.04

NIRSpec

λ (μm)	Ω	N	E_{up}/k_B (K)	I ($\times 10^{-5}$ erg cm^{-2} s^{-1} sr^{-1})
2.718	1/2	3	5414	2.06 ± 0.65
2.851	1/2	1	5314	2.89 ± 1.02
2.870	3/2	1	5134	6.77 ± 1.24
2.886	1/2	2	5401	4.81 ± 0.97
2.901	3/2	2	5250	7.92 ± 0.86
2.922	1/2	3	5541	6.35 ± 0.96
2.934	3/2	3	5415	10.00 ± 0.41
2.960	1/2	4	5735	4.99 ± 0.81
2.970	3/2	4	5627	7.99 ± 0.61
3.000	1/2	5	5982	5.12 ± 0.55
3.008	3/2	5	5888	10.18 ± 0.98
3.048	3/2	6	6199	7.78 ± 0.31
3.085	1/2	7	6632	4.88 ± 0.78
3.091	3/2	7	6558	7.28 ± 1.17
3.131	1/2	8	7033	3.50 ± 0.51
3.136	3/2	8	6966	6.69 ± 1.21
3.179	1/2	9	7483	4.18 ± 0.64
3.183	3/2	9	7422	4.54 ± 0.83
3.229	1/2	10	7483	2.95 ± 0.93

(Top) Intensities of the OH lines detected with MIRI-MRS. (Bottom) Intensities of the OH lines detected with NIRSpec. The uncertainties are calculated by the Python routine curve_fit as 1σ errors on the parameters. The impact of calibration effects is not taken into account and the associated uncertainties can be as high as 20%.

https://doi.org/10.1038/s41550-024-02203-0

Extended Data Table 2 | Intensities of the H_2 lines detected at the bright spot with MIRI-MRS and NIRSpec

λ (μm)	Transition	E_{up}/k_B (K)	I ($\times 10^{-4}$ erg cm^{-2} s^{-1} sr^{-1})
17.035	0-0 S(1)	1015	1.55 ± 0.19
12.279	0-0 S(2)	1682	2.26 ± 0.30
9.665	0-0 S(3)	2504	12.85 ± 0.68
8.025	0-0 S(4)	3474	8.70 ± 2.03
6.910	0-0 S(5)	4586	20.27 ± 0.12
6.109	0-0 S(6)	5830	5.30 ± 0.12
5.511	0-0 S(7)	7197	10.01 ± 0.20
5.053	0-0 S(8)	8677	1.96 ± 0.15
4.695	0-0 S(9)	10262	3.31 ± 0.41
4.410	0-0 S(10)	11940	0.52 ± 0.33
4.181	0-0 S(11)	13703	1.05 ± 0.16
3.846	0-0 S(13)	17444	0.47 ± 0.07
3.724	0-0 S(14)	19403	0.24 ± 0.13
3.626	0-0 S(15)	21412	0.15± 0.09
2.627	1-0 O(2)	5987	9.89 ± 3.15
2.407	1-0 Q(1)	6149	35.70 ± 0.62
2.223	1-0 S(0)	6472	7.06 ± 0.22
2.122	1-0 S(1)	6952	25.03 ± 0.36
2.034	1-0 S(2)	7585	7.04 ± 0.20
1.958	1-0 S(3)	8365	14.23 ± 0.42
1.892	1-0 S(4)	9287	2.87 ± 0.13
1.836	1-0 S(5)	10342	4.16 ± 0.19
1.788	1-0 S(6)	11522	0.42 ± 0.17
1.748	1-0 S(7)	12818	1.06 ± 0.29
2.786	2-1 O(2)	11636	0.65 ± 0.13
2.974	2-1 O(3)	11790	0.64 ± 0.08
2.356	2-1 S(0)	12095	0.20 ± 0.08
2.248	2-1 S(1)	12550	0.52 ± 0.18
2.073	2-1 S(3)	13891	0.47 ± 0.14
2.604	2-1 Q(5)	13891	0.27 ± 0.15
2.654	2-1 Q(7)	15763	0.19 ± 0.08
1.853	2-1 S(7)	18107	0.28 ± 0.19
1.233	3-1 S(1)	17819	0.72 ± 0.10
2.201	3-2 S(3)	19086	0.24± 0.17
2.066	3-2 S(5)	20857	0.16 ± 0.02
3.376	4-3 O(3)	22080	0.10 ± 0.03
1.242	4-2 S(4)	24734	0.15 ± 0.09

The intensities are measured on the not-stitched cubes with the OFF position subtracted. The uncertainties are calculated by the Python routine curve_fit as 1σ errors on the parameters. The impact of calibration effects is not taken into account and the associated uncertainties can be as high as 20%.